Directing entanglement spreading by means of a quantum East/West heterojunction structure

Guanhua Chen ⬤

Department of Physics, South China University of Technology, Guangzhou 510640, China

Yao Yao ⬤*

Department of Physics, South China University of Technology, Guangzhou 510640, China
and State Key Laboratory of Luminescent Materials and Devices, South China University of Technology, Guangzhou 510640, China

We extend the translationally invariant quantum East model to an inhomogeneous chain with East/West heterojunction structure. In analogy to the quantum diffusion of particles, we observe a plateaus-shaped entanglement entropy spreading in the heterojunction during time evolution that can be regarded as continuous cycles in a quantum heat engine. In order to figure out the possibility of manipulating the entanglement entropy as a quantum resource, the entropy growth is shown to be determined by the initial occupation and the site-dependent chemical potential, and the former is equivalent to an effective temperature. Through fine adjustment of these parameters, we discover the entanglement flow is simply superposed with those from two sources of the chain. An intriguing relation between our model and the traditional heat engines is subsequently established.

Introduction. Quantum entanglement, an inherent parameter with nonlocality, has generated much interest as an important physical resource for quantum information processing, metrology, and communication [1–6], which provides a novel concept to study complicated kinetic and dynamic issues [7–10]. In recent studies it was found that the subsystems entanglement entropy as the order parameter in thermalized systems tended to grow rapidly with power-law spreading, while in many-body-localized systems, the propagation of correlation could be confined and the eigenstate thermalization hypothesis is violated, manifesting a more sluggish logarithmic entropy growth [11–15]. The extensive property of entanglement entropy also holds much insightful physics, such as the measurement-induced phase transitions in which the measurement-rate-dependent transitions from volume law to area law have been observed [16–20], and the topological entanglement entropy can be used to detect the topological order [21–23]. In one-dimensional random quantum circuits, the growth of entanglement is explicitly an analogy with stochastic surface growth model of classical particles, and the hydrodynamics can be described by the Kardar-Parisi-Zhang equation [24–26]. In this context it is intuitive to consider feasible ways to efficiently manipulate entanglement entropy in nonthermal systems.

In classical thermodynamics, one is able to manipulate the heat flow by embedding the system into hot and cold baths, but it is difficult to explicitly quantify and direct the relevant entropy flow. In order to extend the classical heat engines to their quantum counterpart, many achievable quantum devices have been theoretically and experimentally studied, such as the thermal diode, thermal transistor, and thermal valve [27–33]. One question which then arises is whether these thermal operations can be formulated within the framework of resource theory for entanglement entropy. The kinetically constrained model (KCM) is a class of model whose dynamics can be quantitatively regulated by the initial states and interaction, providing a candidate for manipulation mechanism [34,35]. The subject of this Letter is thus to control the flow of entanglement entropy in a KCM similar with that for conventional heat current and quantitatively direct the entanglement flows by defining the analogous chemical potential and effective temperature.

Model. We construct a heterojunction based on KCM for the spin-1/2 unidirectional facilitation, e.g., the quantum East model which shows a disorder-free dynamical phase transition [36–38]. The model Hamiltonian is written as

$$H_{\text{east}} = \frac{1}{2} \sum_{i=1}^{N-1} \mu_i n_i - \frac{1}{2} \sum_{i=1}^{N-1} n_i \sigma_{i+1}^x, \tag{1}$$

where $n_i = (\mathbb{1} - \sigma_i^z)/2 = |1\rangle\langle 1|_i$ and $\sigma_i^{x,z}$ are the projector onto the occupied state $|1\rangle$ and Pauli operators at site i. Herein, we use the chemical potential μ_i to replace the common manipulation parameter e^{-s} of thermalization, which is equivalent to the original Hamiltonian [36].

Due to the constrained kinetic terms in the Hamiltonian, there are not conserved particle numbers, and the fast ($0 < \mu_i < 1$) or slow ($\mu_i > 1$) dynamic phase could be observed on two sides of the Rokhsar-Kivelson (RK) point initially defined as a specific value where the ground state is the

*Contact author: yaoyao2016@scut.edu.cn

equal-weight superposition of all dimer states in the quantum dimer model [39,40], suggesting the chemical potential acts as an energy barrier in the chain. In the last few years, for the quantum East model, eigenstate localization properties and the further bosonic East model have been studied in great detail [38,41,42]. This unidirectional constraint has also been extended in the higher-dimensional quantum North-or-East model [43,44], the dynamical phase transition under periodic driving [45,46], and the potential experimental realization in Rydberg platforms [47,48].

In order to construct the chain with heterojunction structure, we add a quantum West model in contact from the right to the chain, and a hopping junction is set between them. The Hamiltonian becomes

$$H = H_{\text{east}} + H_{\text{cont}} + H_{\text{west}}, \qquad (2)$$

with

$$H_{\text{cont}} = -\frac{1}{2}(\sigma_N^+ \sigma_{N+1}^- + \sigma_N^- \sigma_{N+1}^+), \qquad (3)$$

$$H_{\text{west}} = \frac{1}{2} \sum_{i=N+1}^{2N-1} \mu_{i+1} n_{i+1} - \frac{1}{2} \sum_{i=N+1}^{2N-1} \sigma_i^x n_{i+1}. \qquad (4)$$

It can be found that the West part has the same structure with that of the East part but with an inverted facilitation direction. The middle two sites, as ends of respective parts, are symmetrically set as a contact, and their chemical potentials are ignored so that they are dominated by neighboring sites of the East (West) part.

For the sake of generation of current flow, we introduce two regions on each side of the contact: the spacer region with chemical potentials of all sites being set to $\mu_i = \mu_s = 2$ throughout this Letter, and the drive region, unless particularly stated, with chemical potentials being set as $\mu_i = \mu_d = 0.99$, as depicted schematically in Fig. 1(a). The last drive site is also set to $\mu_i = 2$, and we define the number of drive sites D as the drive region size. On the other hand, the occupied state $|1\rangle$ is essential, which serves as the source to facilitate neighboring sites. Since the number of $|1\rangle$ is not conserved, the initial occupied states in the drive region can be regarded as an "effective temperature" related to the dynamics, as discussed below. By this consideration, we initially set all the spacer sites to be $|0\rangle$ (namely, zero temperature), and initial states on the drive sites can be changed with sets of $|0\rangle$ and $|1\rangle$, including superposition states. We define the initial occupation number ρ_0 to quantify the number of $|1\rangle$ in drive regions. For example, a chain with $\mu_1 = \mu_2 = \mu_{2N-1} = \mu_{2N} = 0.99$, $\mu_3 = \cdots = \mu_{2N-2} = 2$ implies $D = 3$, and the eight-site state $|10100000\rangle$ has initial occupation $\rho_0 = 2$ in the East part. Different from the translation-invariant quantum East model with fixed μ_i of every site, the site-dependent μ_i and ρ_0 provide variables to manipulate the imbalanced particle densities flowing in the spacer region. The most advantage of this model is that, since the total number of particle is not conserved, drive regions with initial $|1\rangle$ states can be regarded as sources to generate the steady flow, which is unavailable in systems with conservation of particle number.

However, the ρ_0 and the spreading of particles are not a completely linear relationship. Because of the nearest-neighbor one-spin facilitation of H_{east}, an occupied site may
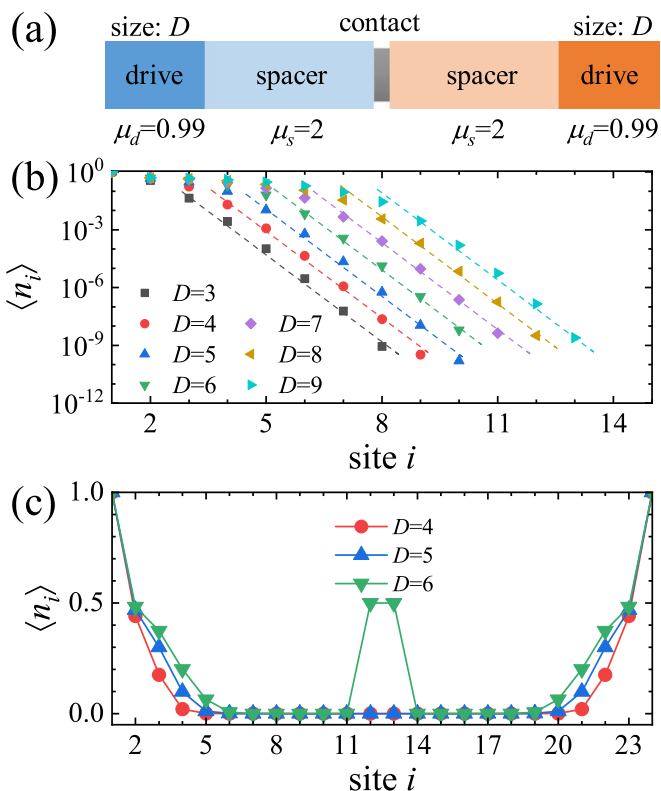

FIG. 1. (a) Schematic illustration of our model with heterojunction structure. East and West parts are marked in blue and orange, respectively. The drive and spacer regions are distinguished by differences in the shade of color. The middle contact interaction is plotted as gray. (b) The simulated mean occupation $\langle n_i \rangle$ of ground states of the quantum East model ($L = 24$, only partial sites are shown) with seven different D's. Exponential decay is observed through the dashed lines of corresponding color. (c) Ground state $\langle n_i \rangle$ of the heterojunction chain with $D = 4$ (red), $D = 5$ (blue), and $D = 6$ (green).

inhibit the next-nearest-neighbor flip. For example, suppose a configuration in three sites of a chain, and the Hamiltonian acting on the state results in

$$H_{\text{east}}|1_1 1_2 0_3\rangle \nearrow |1_1\rangle(\mu|1\rangle - |0\rangle)_2|0_3\rangle, \\ \searrow |1_1 1_2\rangle(-|1\rangle + \mu|0\rangle)_3, \qquad (5)$$

and

$$H_{\text{east}}|0_1 1_2 0_3\rangle \rightarrow |0_1 1_2\rangle(-|1\rangle + \mu|0\rangle)_3, \qquad (6)$$

where $\rightarrow$ figures out subsequent states. In the former case, the first site indirectly inhibits the facilitation of the third site by flipping the second site, which is not the case in the latter. As a result, an occupied site is able to facilitate the nearest neighbor as well as possibly reduce facilitation of further sites. The initial occupation therefore turns out to be worthy of study, which as stated plays the role of a high-temperature source in the drive region.

Results. In the following, we numerically investigate the ground states and dynamics with default size $L = 2N = 24$ by density matrix renormalization group (DMRG, the maximum bond dimension is set as 300) and time-evolving block decimation (TEBD, the Trotter gate time step and truncation error threshold are set as $\Delta t = 0.05$ and 10^{-9}) methods in open boundary conditions (OBC) [49–51]. Based on previous research, the ground state of the translation-invariant quantum East model for $\mu_i > 1$ shows that occupied sites are localized at the first few sites. That is, the expectation value of n_i exponentially decays as $\langle n_i \rangle \sim e^{-i/\xi}$, with the localization length ξ depending on μ_i [38]. By contrast, a homogeneous occupation distribution is present in thermal phase ($\mu_i < 1$ or $s < 0$). By adding nonuniform μ_i to the quantum East model, in Fig. 1(b), we show the mean occupation $\langle n_i \rangle$ as a function of sites i with different D. The fitting dashed lines which figure out the decay rates have exactly the same slope because of the same $\mu_s = 2$ in the spacer region. On the other hand, as illustrated by Fig. 1(c), by changing the number of drive sites up to $D = 6$ in the heterojunction model, the particles are found to accumulate in the middle of the chain. It implies that the enlarged drive region can not only increase the occupation in the drive region but also enforce the particles injecting onto the surface of spacer region, similar with the function of gate voltage in conventional field-effect transistors [52]. Along with the investigation of the particle injection in systems of different sizes (see Appendix A), we conclude that the greater chemical potential μ_s (equivalent to smaller localization length ξ) forces particles to localize around drive regions and holds back the injection, while enlarging drive size D could promote injection.

For investigating this injection of particles in a dynamical manner, we construct unipolar initial states which only the sites in East drive region are occupied and the evolution of the West part can thus be ignored. More complicated bipolar structures adding occupation of both parts will be discussed in a later section. As mentioned in Ref. [38], the Hilbert space of the quantum East model is determined by the first occupied site, which is normally set as the leftmost and vice verse for the West model. Here, we show the unipolar evolution of the initial state $\rho_0 = 3$, $D = 3$, namely, $|111\,000\ldots00\rangle$. As shown in Fig. 2(a), the dynamics of $\langle n_i \rangle$ reveals a slow diffusion process. The particles firstly accumulate at the leftmost site, and later a periodic wave motion is clearly visible.

Next, we explore the entanglement spreading by considering the entropy cut at every bond of the chain, namely, $S_r = -\mathrm{Tr}_r \varrho \log \varrho$, with ϱ being the reduced density matrix taking a partial trace at $i = r$, which differs from the common half-chain entanglement entropy and has been used to study the entanglement transition related to the quantum Zeno effect [53]. In Fig. 2(b) the entanglement entropy manifests similar evolution features with that of mean occupations, that is, there are four periods of oscillation up to around $t \sim 350$. In order to be more detailed on these similar variation tendencies, we plot the $\langle n_{L/2} \rangle$ and half-chain entropy $S_{L/2}$ in the insets of Fig. 2. It is clear that they share almost the same growth process, resulting from the blocking effect of H_{cont} on the entanglement spreading. Since the evolution on the sites from $i = L/2 + 2$ to L can be ignored, the reduced density matrix after partial tracing of the left half chain is totally determined
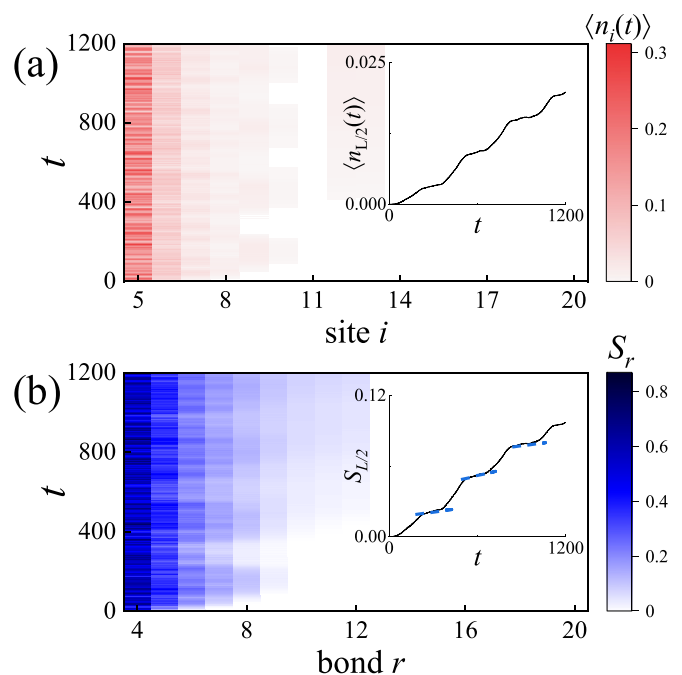

FIG. 2. Dynamics of initial state as $|11100\ldots000\rangle$ for $D = 3$. (a) Time evolution of occupation $\langle n_i \rangle$. The growth of the middle site $\langle n_{L/2} \rangle$ is specifically shown in the inset. (b) The von Neumann entropy S_r of every bond r, i.e., the subsystem of the reduced density matrix is chosen based on the cut between $i = r$ and $i = r + 1$. The bipartition entanglement evolution of the middle bond $S_{L/2}$ is present in the inset, and three slow growth stages are marked with blue dashed lines.

by the site $i = L/2 + 1$. That is, in terms of the property of entanglement entropy, $S_{L/2}$ can only depend on $\langle n_{L/2+1} \rangle$ (and also $\langle n_{L/2} \rangle$ in terms of the hopping junction). This entanglement growth reminds us of the surface growth model for entanglement in random quantum circuits, where an entanglement tsunami can be described by the Kardar-Parisi-Zhang (KPZ) equation of particles [24,54,55].

Moreover, the wavelike entanglement spreading from the left accumulates at junction, with rate varying periodically, generating a staged entropy growth, which means the crests are associated with maximums of growth rate, and every trough resulting in the slow quasi-isentropic processes (marked with blue dashed lines). This oscillatory behavior of entanglement entropy can be regarded as continuous cycles of heat engine described by a temperature-entropy diagram. We further calculate the entropy growth of systems of different sizes, which solely shows that the entanglement of a smaller system is easier to approach middle junction.

The above results imply that we may be able to manipulate entanglement analogous to enabling the particle flow with a series of variables like the potential difference. Here, the occupation of drive region standing for temperature provides a possible role to manipulate entanglement, which deserves further study based on the previous analysis. To this end, we then focus on the influence of initial occupation and drive size on $S_{L/2}$, which has been discussed a bit based on the maximal number of consecutive down spins in Ref. [36]. With the single-site superposition state $|\alpha\rangle_i = \sqrt{\alpha}|1\rangle_i + \sqrt{1-\alpha}|0\rangle_i$,
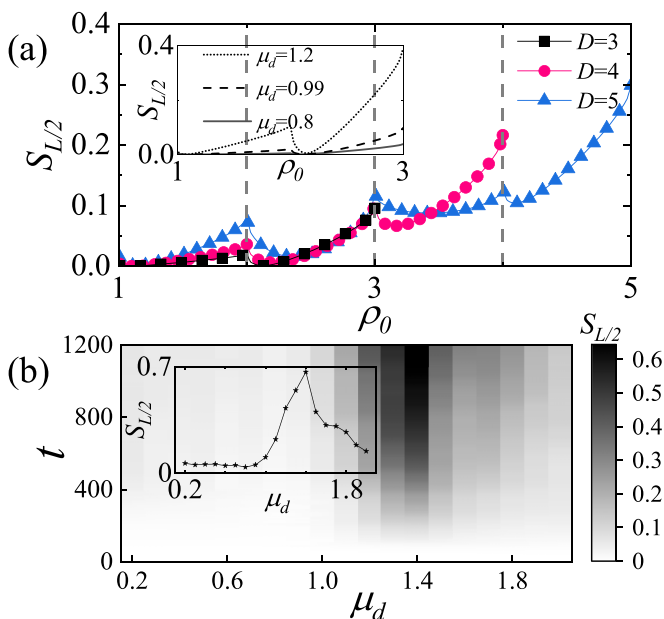
FIG. 3. The entanglement entropy under different conditions in the heterojunction. (a) The $S_{L/2}$ at $t = 1200$ as a function of the initial occupation ρ_0 with $D = 3$ (black square), $D = 4$ (pink circle), and $D = 5$ (blue triangle). As in Eq. (7), the ρ_0 increases by sweeping $\alpha \in [0, 1]$ between integers x. Local maximum values at integer ρ_0 are marked with dashed lines. Inset: Comparison among three μ_i in the drive region for $D = 3$. (b) The evolution of $S_{L/2}$ with initial state $|11100\ldots\rangle$ as a function of $\mu_1 = \mu_2 = \mu_d$. Inset: The final states $S_{L/2}$ at $t = 1200$.

we construct a series of continuous nonintegral ρ_0 at the $(x + 1)$-th site for unipolar initial states as

$$|\phi(x, \alpha)\rangle = |1_1 1_2 \ldots 1_x\rangle|\alpha\rangle_{x+1}|0_{x+2} \ldots 0_{L-1} 0_L\rangle, \quad (7)$$

so that the initial occupation becomes $\rho_0 = x + \alpha$. Take an example: $|\phi(3, 1/3)\rangle = |111\rangle(\sqrt{1/3}|1\rangle + \sqrt{2/3}|0\rangle)|000\ldots\rangle$. Figure 3(a) illustrates $S_{L/2}$ vs ρ_0 at $t = 1200$ with different D. It is observed that every local maximum appears at integral ρ_0 (marked with dashed lines). It should be noted that the fastest entropy change of every D appears at the final stage (such as $\rho_0 \in [4, 5]$ for $D = 5$), suggesting the entropy increase is mainly related to the boundary between the drive and spacer region. More interestingly, as the initial occupation increases, $S_{L/2}$ shows small downward tendencies and will reach local minima, which are balanced points between inhibition and facilitation. When the ρ_0 increases further, the facilitation plays a leading role until the next integer. As mentioned above, the ρ_0 could be regarded as an effective temperature with respect to the "cold" spacer region, so Fig. 3(a) can be regarded as an entropy-temperature diagram for the heat engine whose cycles can be approximately constituted by isentropic and isothermal stages. By an isentropic process we mean stages where entropy is almost constant when ρ_0 increases, which are always found around the local minima, namely, these balanced points. Then the isothermal process refers to stages where entropy changes so rapidly that we can regard ρ_0 as almost static, which are always peaked at around integer ρ_0. This effective temperature then serves as

the essential point of our model as we find a way to define a temperature gradient relevant to dynamical characters in a quantum heat engine. One may doubt above results seem to be strongly model dependent, but the East model as the simplest paradigm with a facilitated interaction as well as an occupation potential term can be extended to many more sophisticated models without particle conservation [56,57]. The definition of temperature here in a dynamic perspective can be generalized to other KCMs with facilitation. We also compute different μ_d of the drive region in the inset, which shows similar variation tendencies with a slight difference of amplitude.

One may ask if the chemical potential μ_d has the same effect of temperature. We then fix the $D = 3$, $\rho_0 = 3$ and show the entropy variance as a function of μ_d in the drive region in Fig. 3(b). The entanglement does not change with μ_d when $\mu_d < 1.0$ and then increases when $1.0 < \mu_d < 1.4$. Crossing a turning point, the smaller μ_d enables more active facilitation and more easily spreading entanglement. As addressed above, a possible phase transition is supposed to appear at the critical point $\mu_d = 1$ for fast and slow dynamics, but the fastest-growing entropy as well as the turning point is observed at around $\mu_d = 1.4$. This result can be qualitatively interpreted by dividing the parameter extent of μ_d into three sectors. When $\mu_d < 1$, the spacer region is attached to a thermalized drive region where few particles can be pumped into the localized spacer region. For larger $\mu_d > 2$, the drive region freezing most particles is relatively more localized than the spacer region and the entanglement flow is thus blocked. Then there is a competition between two sectors in the middle interval $\mu_d \in [1, 2]$, where particles not only stay at the weakly localized drive region but also can be pumped into the spacer region. That is, what matters is not the turning point around $\mu_d = 1.4$ but the interplay of three sectors. More numerical results for $\mu > 2$ and $D = 4$ are available in Appendix B. Consequently, the chemical potential in our model cannot be equivalently recognized as the temperature showing an approximately positive correlation with entropy like ρ_0; it is more like a parameter of detuning.

Hence, now we have two parameters to regulate the growth of entanglement flows. As seen in Fig. 2, the entropy flow shows apparent periodic waves whose amplitude and period are related to ρ_0 and μ_d. Concretely, we would like to present two illustrative examples of coupling between entanglement flows from two sides in the form of waves: one involving the same flow tendencies but with varying amplitudes, and the other one showcasing similar amplitudes with different tendencies. After some tentative simulations, we have elaborately chosen initial conditions appropriate for analysis. We set the initial state as $|11100\ldots00101\rangle$ (the initial state $|1010\ldots\rangle$ is discussed in more detail in Appendix C) and plot the resulting S_r in Fig. 4(a). Even though two flows have the same tendency from equal μ_d, they have unequal amplitudes, and the West part shows an evidently faster entanglement flow than that in the East part. This amplitude difference could be explained by previous discussion that the second unoccupied site hinders the flip of the edge occupied site of $|1_3\rangle$, which matters most to the pump spacer region during evolution. The $S_{L/2}$ values of three different initial states as a bipolar and two unipolar evolutions are further displayed in Fig. 4(b). Three curves
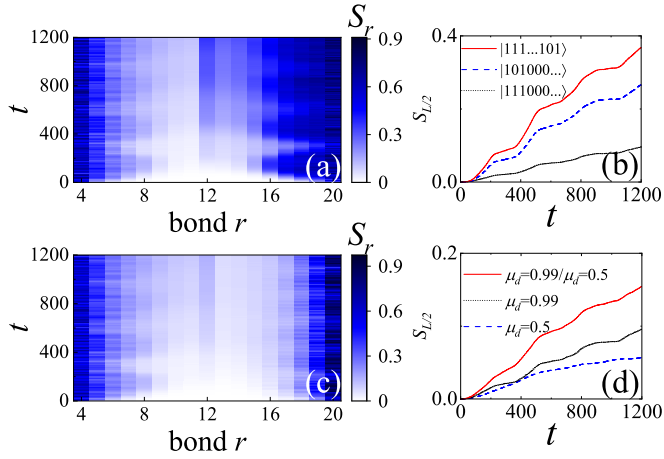
FIG. 4. Dynamics of entropy S_r for the heterojunction chain. (a) The initial state is chosen as $|11100\ldots00101\rangle$ with $D = 3$ and $\mu_d = 0.99$. (c) The initial state is chosen as $|11100\ldots00111\rangle$ with $D = 3$, $\mu_d = 0.99$ in the East model and $\mu_d = 0.5$ in the West model. Comparisons of $S_{L/2}$ under different conditions are plotted in (b) and (d).

have similar cyclic growth processes, and interestingly, the red curve is equivalent to the superposition of the other two, which is qualitatively attributed to the extensive property of entropy. It is also worth noting that the extensivity heavily depends on the choice of model. For our heterojunction structure, the unidirectional facilitation imposes the direction of entanglement, and the hopping contact in Eq. (3) which makes the middle two sites a coupled zone between two parts provides a possible interaction to combine the entropy of two inverted models. Namely, the junction gathers not only the particles but also entanglement. In addition, we calculate the evolution under two different dynamical parameters, $\mu_d = 0.99$ in the East and $\mu_d = 0.5$ in the West, as shown in Fig. 4(c). Here, a lower μ_d brings a different flow tendency, that is, a coupling between similar amplitudes. A simple superposition is also found in Fig. 4(d).

Discussion and conclusion. Before ending, we discuss more on the chemical potential and temperature. In our model we replace the flip factor e^{-s} in the common quantum East model with parameter μ_i as the chemical potential for the occupation n_i in Hamiltonian Eq. (1). As is well known, in the traditional thermodynamics, the internal energy of ideal gases can be described by the Euler equation as

$$E = TS - PV + \sum_j \mu_j N_j, \tag{8}$$

where N_j denotes the particle number of the jth component and μ_j the relevant chemical potential. In an electrochemical cell, the difference of chemical potential serves as the bias voltage to generate current flow. In the quantum East model, however, the chemical potential difference plays a more complicated dualistic role in dynamics. Here, the non-conservation of particles from the facilitation term provides a persistent particle flow almost identical with the entanglement flow analogous to the steady heat flow from the hot to cold region, which suggests a way to understand the relationship between the classical and quantum heat engine. Most

importantly, since in normal cases the latter engine is based upon pure states, it is difficult to define a relevant temperature analogous to its classical counterpart. Here in our model, the drive region size and initial occupation together play the role of temperature, which can be promisingly applied to redefine the temperature in quantum heat engines.

In summary, we have studied a nonuniform one-dimensional KCM based on the nearest-neighbor-facilitated quantum East model. We focus on the dynamics of entanglement spreading and explore its potential of realizing entanglement manipulation. The entanglement flows depending on the initial states and drive region are investigated. Through introducing an analogical West model to construct a heterojunction, the superposed entanglement flows are studied and the relationship with quantum heat engines is discussed. Further, our work offers a different perspective on KCMs with facilitation and opens up possibilities for research of entanglement dynamics within the framework of thermodynamics.

Appendix A: Ground-state particle injection. In the main text we found the particle injection in the contact sites is determined by the drive region size D. Here, we assume a linear inequality as the injection condition,

$$a_1 D + a_2 \xi \geqslant L/2, \tag{A1}$$

where ξ and L label the localization length and the total number of sites, and a_1 and a_2 are desired fitting coefficients.

According to previous research about the quantum East model, the localization length only depends on the chemical potential μ_i of the spacer region (set as μ_s in the following), and it can be derived that $\xi \propto (\log\mu_s)^{-0.533}$ from Ref. [38]. In Fig. 5 we thus compute the critical μ_s, generating just the particle injection of the ground state [the equality holds in Eq. (A1)] as a function of drive region size D and plot the corresponding linear fit of ξ. These results can be well fitted by Eq. (A1), and we get $a_1 = 0.95$, $a_2 = 24.86$ by averaging five different L. That is, the particle injection arises when

$$0.95D + 24.86\xi \geqslant L/2. \tag{A2}$$

To verify the validity of the above equation, the ξ/L is plotted against D/L in the inset of Fig. 5(b). It can be observed that all five curves stay around the resulting injection condition,

$$0.95D/L + 24.86\xi/L \geqslant 1/2, \tag{A3}$$

that is, they are collapsed onto a single curve well. Additionally, at fixed D/L with infinite L, the ξ also has to be infinity as in Eq. (A3), which indicates the critical chemical potential is trending to the RK point of slow dynamics $\mu_s = 1$, as shown in the inset of Fig. 5(a).

It is worth mentioning that changing the chemical potential of the drive region also delivers different outcomes, but the impact is very slight when the drive region size is small.

Appendix B: Entanglement flow under varying chemical potentials. As we state and discuss in the main text, the unexpected change in entropy $S_{L/2}$ with chemical potential μ_d is attributed to three sectors with different localization properties.
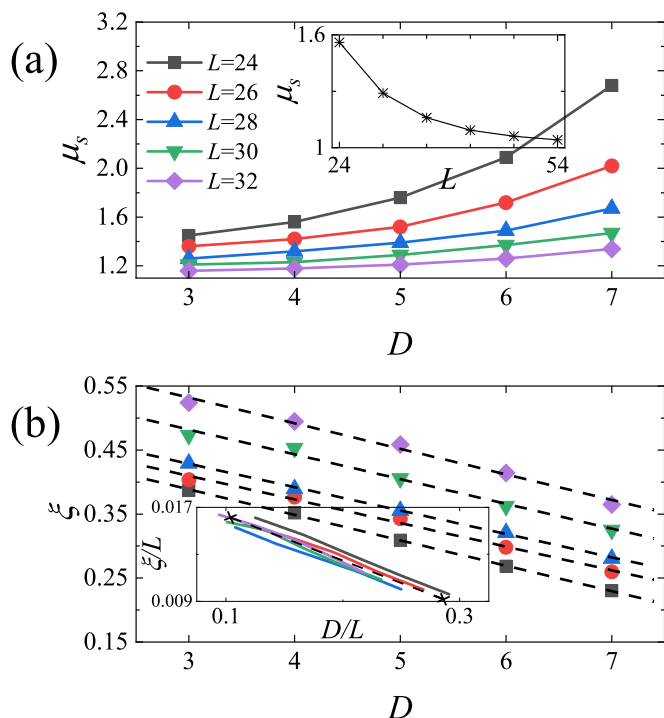
FIG. 5. (a) Critical μ_s as a function of D for ground states of the heterojunction model with different system sizes L. Inset: Critical μ_s at fixed $D/L = 1/6$ with increasing L. (b) The localization length ξ are obtained from corresponding μ_s, and the dashed lines are the linear fit. Inset: ξ/L as a function of D/L, and Eq. (A2) in equality holding is plotted by the dashed line with crosses.

FIG. 6. The final states $S_{L/2}$ at $t = 1200$ as a function of μ, the chemical potential in drive region (a) $D = 3$ with initial occupation number $\rho_0 = 2, 3$ and (b) $D = 4$ with initial occupation number $\rho_0 = 1, 2, 3$.

In Fig. 6(a) we plot the final $S_{L/2}$ under $D = 3$ related to μ with initial states $\rho_0 = 2 : |1100\ldots\rangle$ and $\rho_0 = 3 : |11100\ldots\rangle$, as examples to show the physical significance. For $\mu_d < 1$, the drive region exhibits the thermalized phase, and fewer particles can be facilitated to break through the edge between two regions. As μ_d increases to approach the localization transition point $\mu_d = 1$, a slight growth is observed. If enlarging $\mu_d > \mu_s = 2$, the drive region is more localized than the spacer region, and most particles are frozen; hence corresponding entropy flow is inhibited. In the interval $1 < \mu_d < 2$ called weak localization, though the spacer region is relatively more localized, a competition between two sectors exists, which leads to the crossover at around $\mu_d = 1.4$ for both initial states. Three sectors are labeled in the figure. Different curves of ρ_0 have a similar tendency, and the $\rho_0 = 3$ shows a larger amplitude, resulting from the edge occupation of the drive region, which mostly affects the facilitation of sites in the spacer region.

Additionally, a larger drive region and more initial occupation possibly make the relation between μ_d and entanglement so complicated that it is hard to quantitatively predict the entanglement growth. However, some common characters can also be noticed in Fig. 6(b), a larger drive region $D = 4$ with different initial states. For $\rho_0 = 1 : |100\ldots\rangle$, large μ_d has effectively limited the facilitation of the sites in the drive region, and little entropy can flow to the contact as shown in the figure. By the way, a similar situation also exists in $D = 3$ but is not obvious. In the sector of weak localization, a maximum
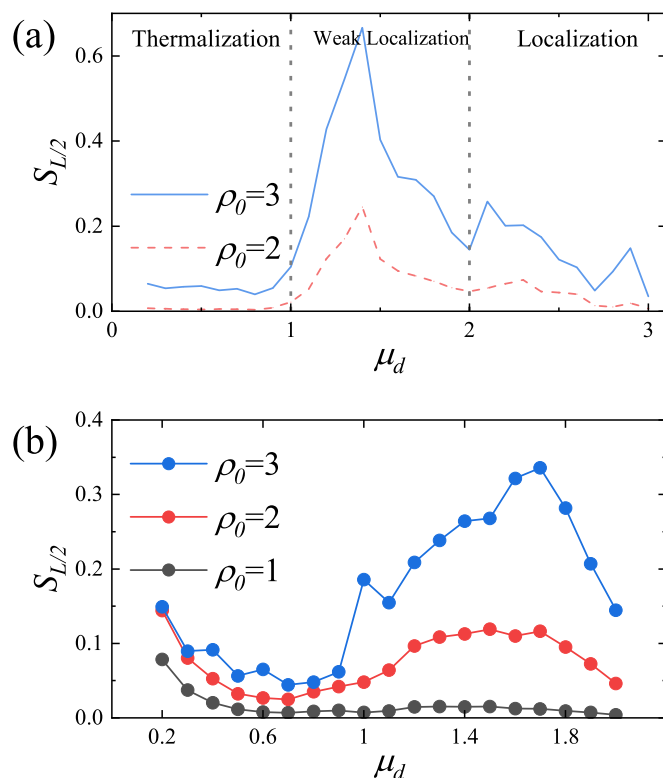
is identified at around $\mu_d = 1.7$ from the competition noted above.

Appendix C: Discontinuous occupation initial states. We have discussed initial states $|\phi(x, \alpha)\rangle$ with continuous occupation in the main text, and in this section, the initial state with discontinuous occupation will be analyzed based on $|10100\ldots\rangle$. Here, we construct initial superposition states as

$$|b\rangle = \sqrt{b}|1110\ldots\rangle + \sqrt{1-b}|1010\ldots\rangle, \qquad (C1)$$

where b is the superposition coefficient. Figure 7 illustrates the final $S_{L/2}$ vs b, and we identify a curve akin to the behavior of the entropy-temperature diagram in the main text. Referring
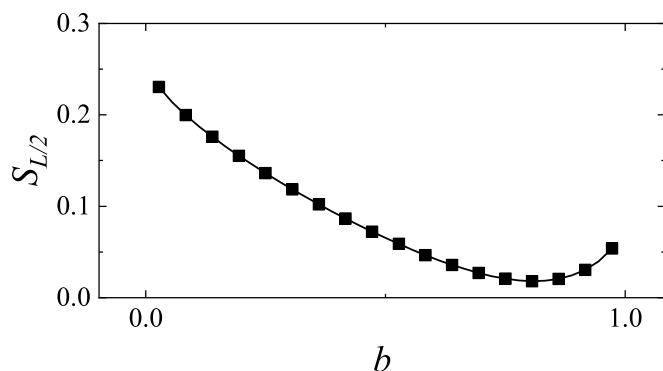

FIG. 7. The $S_{L/2}$ at $t = 1200$ as a function of the superposition coefficient b under $D = 3$ and $\mu = 0.99$.

to the previous results, in the first stage (before the red circle), the inhibition plays a dominant role during the increase of the second occupation. As the occupation continues to increase, the facilitation from the second sites is starting to perform

stronger than inhibition, and thus the entropy grows after the minimum. This result also verifies the dual role of the occupied site in the East model, including facilitation and inhibition.

---

[1] R. Horodecki, P. Horodecki, M. Horodecki, and K. Horodecki, Quantum entanglement, Rev. Mod. Phys. **81**, 865 (2009).

[2] M. F. Riedel, P. Böhi, Y. Li, T. W. Hänsch, A. Sinatra, and P. Treutlein, Atom-chip-based generation of entanglement for quantum metrology, Nature (London) **464**, 1170 (2010).

[3] V. Giovannetti, S. Lloyd, and L. Maccone, Advances in quantum metrology, Nat. Photonics **5**, 222 (2011).

[4] G. Tóth and I. Apellaniz, Quantum metrology from a quantum information science perspective, J. Phys. A: Math. Theor. **47**, 424006 (2014).

[5] F. Flamini, N. Spagnolo, and F. Sciarrino, Photonic quantum information processing: A review, Rep. Prog. Phys. **82**, 016001 (2019).

[6] E. Chitambar and G. Gour, Quantum resource theories, Rev. Mod. Phys. **91**, 025001 (2019).

[7] C. J. Turner, A. A. Michailidis, D. A. Abanin, M. Serbyn, and Z. Papić, Weak ergodicity breaking from quantum many-body scars, Nat. Phys. **14**, 745 (2018).

[8] Z. Lan, M. van Horssen, S. Powell, and J. P. Garrahan, Quantum slow relaxation and metastability due to dynamical constraints, Phys. Rev. Lett. **121**, 040603 (2018).

[9] M. Ostmann, M. Marcuzzi, J. P. Garrahan, and I. Lesanovsky, Localization in spin chains with facilitation constraints and disordered interactions, Phys. Rev. A **99**, 060101(R) (2019).

[10] A. Lerose, F. M. Surace, P. P. Mazza, G. Perfetto, M. Collura, and A. Gambassi, Quasilocalized dynamics from confinement of quantum excitations, Phys. Rev. B **102**, 041118(R) (2020).

[11] J. H. Bardarson, F. Pollmann, and J. E. Moore, Unbounded growth of entanglement in models of many-body localization, Phys. Rev. Lett. **109**, 017202 (2012).

[12] M. Serbyn, Z. Papić, and D. A. Abanin, Universal slow growth of entanglement in interacting strongly disordered systems, Phys. Rev. Lett. **110**, 260601 (2013).

[13] D. A. Huse, R. Nandkishore, and V. Oganesyan, Phenomenology of fully many-body-localized systems, Phys. Rev. B **90**, 174202 (2014).

[14] R. Fan, P. Zhang, H. Shen, and H. Zhai, Out-of-time-order correlation for many-body localization, Sci. Bull. **62**, 707 (2017).

[15] R. Nandkishore and D. A. Huse, Many-body localization and thermalization in quantum statistical mechanics, Annu. Rev. Condens. Matter Phys. **6**, 15 (2015).

[16] B. Skinner, J. Ruhman, and A. Nahum, Measurement-induced phase transitions in the dynamics of entanglement, Phys. Rev. X **9**, 031009 (2019).

[17] Q. Tang and W. Zhu, Measurement-induced phase transition: A case study in the nonintegrable model by density-matrix renormalization group calculations, Phys. Rev. Res. **2**, 013022 (2020).

[18] E. Granet, C. Zhang, and H. Dreyer, Volume-law to area-law entanglement transition in a nonunitary periodic Gaussian circuit, Phys. Rev. Lett. **130**, 230401 (2023).

[19] J. M. Koh, S.-N. Sun, M. Motta, and A. J. Minnich, Measurement-induced entanglement phase transition on a superconducting quantum processor with mid-circuit readout, Nat. Phys. **19**, 1314 (2023).

[20] Y. L. Gal, X. Turkeshi, and M. Schirò, Volume-to-area law entanglement transition in a non-Hermitian free fermionic chain, SciPost Phys. **14**, 138 (2023).

[21] H.-C. Jiang, Z. Wang, and L. Balents, Identifying topological order by entanglement entropy, Nat. Phys. **8**, 902 (2012).

[22] N. Laflorencie, Quantum entanglement in condensed matter systems, Phys. Rep. **646**, 1 (2016).

[23] B. Zeng, X. Chen, D.-L. Zhou, X.-G. Wen *et al.*, *Quantum Information Meets Quantum Matter* (Springer, New York, 2019).

[24] A. Nahum, J. Ruhman, S. Vijay, and J. Haah, Quantum entanglement growth under random unitary dynamics, Phys. Rev. X **7**, 031016 (2017).

[25] D. Bernard and P. L. Doussal, Entanglement entropy growth in stochastic conformal field theory and the KPZ class, Europhys. Lett. **131**, 10007 (2020).

[26] M. P. Fisher, V. Khemani, A. Nahum, and S. Vijay, Random quantum circuits, Annu. Rev. Condens. Matter Phys. **14**, 335 (2023).

[27] A. Marcos-Vicioso, C. López-Jurado, M. Ruiz-Garcia, and R. Sánchez, Thermal rectification with interacting electronic channels: Exploiting degeneracy, quantum superpositions, and interference, Phys. Rev. B **98**, 035414 (2018).

[28] K. Joulain, J. Drevillon, Y. Ezzahri, and J. Ordonez-Miranda, Quantum thermal transistor, Phys. Rev. Lett. **116**, 200601 (2016).

[29] W.-R. Zhong, D.-Q. Zheng, and B. Hu, Thermal control in graphene nanoribbons: Thermal valve, thermal switch and thermal amplifier, Nanoscale **4**, 5217 (2012).

[30] R. Kosloff and A. Levy, Quantum heat engines and refrigerators: Continuous devices, Annu. Rev. Phys. Chem. **65**, 365 (2014).

[31] J. P. S. Peterson, T. B. Batalhão, M. Herrera, A. M. Souza, R. S. Sarthour, I. S. Oliveira, and R. M. Serra, Experimental characterization of a spin quantum heat engine, Phys. Rev. Lett. **123**, 240601 (2019).

[32] A. Gubaydullin, G. Thomas, D. S. Golubev, D. Lvov, J. T. Peltonen, and J. P. Pekola, Photonic heat transport in three terminal superconducting circuit, Nat. Commun. **13**, 1552 (2022).

[33] J. Klatzow, J. N. Becker, P. M. Ledingham, C. Weinzetl, K. T. Kaczmarek, D. J. Saunders, J. Nunn, I. A. Walmsley, R. Uzdin, and E. Poem, Experimental demonstration of quantum effects in the operation of microscopic heat engines, Phys. Rev. Lett. **122**, 110601 (2019).

[34] F. Ritort and P. Sollich, Glassy dynamics of kinetically constrained models, Adv. Phys. **52**, 219 (2003).

[35] J. P. Garrahan, Aspects of non-equilibrium in classical and quantum systems: Slow relaxation and glasses, dynamical large

deviations, quantum non-ergodicity, and open quantum dynamics, Physica A **504**, 130 (2018).

[36] M. van Horssen, E. Levi, and J. P. Garrahan, Dynamics of many-body localization in a translation-invariant quantum glass model, Phys. Rev. B **92**, 100305(R) (2015).

[37] M. C. Bañuls and J. P. Garrahan, Using matrix product states to study the dynamical large deviations of kinetically constrained models, Phys. Rev. Lett. **123**, 200601 (2019).

[38] N. Pancotti, G. Giudice, J. I. Cirac, J. P. Garrahan, and M. C. Bañuls, Quantum east model: Localization, nonthermal eigenstates, and slow dynamics, Phys. Rev. X **10**, 021051 (2020).

[39] D. S. Rokhsar and S. A. Kivelson, Superconductivity and the quantum hard-core dimer gas, Phys. Rev. Lett. **61**, 2376 (1988).

[40] C. Castelnovo, C. Chamon, C. Mudry, and P. Pujol, From quantum mechanics to classical statistical physics: Generalized Rokhsar–Kivelson Hamiltonians and the "Stochastic Matrix Form" decomposition, Ann. Phys. **318**, 316 (2005).

[41] R. J. Valencia-Tortora, N. Pancotti, and J. Marino, Kinetically constrained quantum dynamics in superconducting circuits, PRX Quantum **3**, 020346 (2022).

[42] A. Geißler and J. P. Garrahan, Slow dynamics and nonergodicity of the bosonic quantum east model in the semiclassical limit, Phys. Rev. E **108**, 034207 (2023).

[43] C. Casert, T. Vieijra, S. Whitelam, and I. Tamblyn, Dynamical large deviations of two-dimensional kinetically constrained models using a neural-network state ansatz, Phys. Rev. Lett. **127**, 120602 (2021).

[44] L. Causer, M. C. Bañuls, and J. P. Garrahan, Optimal sampling of dynamical large deviations in two dimensions via tensor networks, Phys. Rev. Lett. **130**, 147401 (2023).

[45] C. M. Dai, Y. Zhang, and X. X. Yi, Driving induced ergodicity breaking in a kinetic constraint quantum system, J. Phys. B: At., Mol. Opt. Phys. **55**, 235001 (2022).

[46] B. Bertini, P. Kos, and T. Prosen, Localized dynamics in the Floquet quantum east model, Phys. Rev. Lett. **132**, 080401 (2024).

[47] P. Kitson, T. Haug, A. L. Magna, O. Morsch, and L. Amico, Rydberg atomtronic devices, arXiv:2310.18242.

[48] R. J. Valencia-Tortora, N. Pancotti, M. Fleischhauer, H. Bernien, and J. Marino, Rydberg platform for nonergodic chiral quantum dynamics, Phys. Rev. Lett. **132**, 223201 (2024).

[49] G. Vidal, Classical simulation of infinite-size quantum lattice systems in one spatial dimension, Phys. Rev. Lett. **98**, 070201 (2007).

[50] U. Schollwöck, The density-matrix renormalization group in the age of matrix product states, Ann. Phys. **326**, 96 (2011), January 2011 Special Issue.

[51] M. Fishman, S. R. White, and E. M. Stoudenmire, The ITensor Software Library for tensor network calculations, SciPost Phys. Codebases, 4 (2022).

[52] D. Neamen, *Semiconductor Physics and Devices* (McGraw-Hill, Inc., New York, 2002).

[53] Y. Li, X. Chen, and M. P. A. Fisher, Quantum Zeno effect and the many-body entanglement transition, Phys. Rev. B **98**, 205136 (2018).

[54] T. Sasamoto and H. Spohn, One-dimensional Kardar-Parisi-Zhang equation: An exact solution and its universality, Phys. Rev. Lett. **104**, 230602 (2010).

[55] H. Liu and S. J. Suh, Entanglement tsunami: Universal scaling in holographic thermalization, Phys. Rev. Lett. **112**, 011601 (2014).

[56] J. M. Hickey, S. Genway, and J. P. Garrahan, Signatures of many-body localisation in a system without disorder and the relation to a glass transition, J. Stat. Mech. (2016) 054047.

[57] L. Causer, I. Lesanovsky, M. C. Bañuls, and J. P. Garrahan, Dynamics and large deviation transitions of the XOR-Fredrickson-Andersen kinetically constrained model, Phys. Rev. E **102**, 052132 (2020).